Electrochimica Acta 55 (2010) 8938–8946

Contents lists available at ScienceDirect

Electrochimica Acta

journal homepage: www.elsevier.com/locate/electacta

Oxygen reduction reaction on electrodeposited $Pt_{100-x-y}Ni_xPd_y$ thin films

Sun-Mi Hwang[a,b], Chang Hwa Lee[a], Jae Jeong Kim[b], Thomas P. Moffat[a,*]

[a] Materials Science and Engineering Laboratory, National Institute of Standards and Technology, 100 Bureau Drive, Mail Stop 8551, Gaithersburg, MD 20899, United States
[b] School of Chemical and Biological Engineering, Seoul National University, San 56-1, Sillim-dong, Gwanak-gu, Seoul 151-744, Republic of Korea

ARTICLE INFO

Article history:
Received 7 June 2010
Received in revised form 30 July 2010
Accepted 3 August 2010
Available online 10 August 2010

Keywords:
Electrocatalysis
Electrodeposition
Pt alloys
PtNiPd
Oxygen reduction reaction (ORR)

ABSTRACT

The kinetics of the oxygen reduction reaction (ORR) were examined on a series of $Pt_{100-x-y}Ni_xPd_y$ ternary alloys. Films were produced by electrodeposition that involved a combination of underpotential and overpotential reactions. For Pt-rich $Pt_{100-x-y}Ni_xPd_y$ alloy films ($x < 0.65$) Ni co-deposition occurred at underpotentials while for Ni-rich films ($x > 0.65$) deposition proceeded at overpotentials. Rotating disk electrode (RDE) measurements of the ORR kinetics on Ni-rich $Pt_{100-x-y}Ni_xPd_y$ thin films revealed up to ~6.5-fold enhancement of the catalytic activity relative to Pt films with the same Pt mass loading. More than half of the electrocatalytic gain may be attributed to surface area expansion due to Ni dealloying. Surface area normalization based on the H_{upd} charge reduced the enhancement factor to a value less than 2. The most active ternary alloy film for ORR was $Pt_{25}Ni_{73}Pd_2$. Comparison of the ORR on Pt, $Pt_{20}Ni_{80}$, $Pt_{25}Ni_{73}Pd_2$ thin films indicate that the binary alloy is the most active with a H_{upd} normalized ORR enhancement factor of up to 3.0 compared to 1.6 for the ternary alloy.

Published by Elsevier Ltd.

1. Introduction

Platinum is the conventional catalyst for hydrogen oxidation reaction (HOR) and/or oxygen reduction reaction (ORR) in polymer electrolyte membrane fuel cells (PEMFCs). However, the sluggish oxygen reduction reaction (ORR) associated with Pt cathodes in PEMFC is one of the critical limitations hindering commercialization. The high cost combined with limited performance, durability, and susceptibility to poisoning, remain major barriers to the utilization of pure Pt. Consequently, significant research is underway exploring the activity and utility of various platinum-based binary (PtM, M = Co, Ni, Fe, Cu, Cr, etc.) or ternary alloys (PtM_1M_2, $M_{1,2}$ = Co, Ni, Fe, Cu, Cr, Zr, Mn, etc.) [1–30]. Generally speaking many of these alloys have been shown to improve the ORR activity compared to unalloyed Pt by a factor that typically ranges between 2 and 4. Even more encouraging, $Pt_3Ni(1\,1\,1)$ single crystals have been reported to be 10-fold more active than Pt(1 1 1) and 90-fold more active than state-of-the-art Pt/C catalyst [6]. Looking beyond Pt-based alloys, Pd has been examined as a Pt substitute based on its similar physical properties that arise from the periodicity of elements [1,2,17–28]. However, detailed investigations have revealed that Pd has lower activity and stability towards the ORR. As with Pt, alloying Pd with other metals, M, Pd-M (M = Ni, Pt, Fe, Cu, Co, W, Sn, V, Au etc.) has been shown to be an effective strategy to substantially improve upon these limitations [1,2,16–29]. Although the reason for the superior behavior exhibited by various Pd-M (M = Ni, Fe, Co, Pt) or Pt-M (M = Co, Ni, Cr, Mn, V) alloys is still debated, it is thought to be associated with perturbation of the electronic state and geometry of a Pt enriched surface layer by the underlying alloy [1,6–8,19]. This is often discussed in terms of electronic effects (d-band electron vacancy), geometric factors (Pt–Pt bond distance), surface composition, and/or atomic ordering. Models continue to be developed and evaluated with ever more sophistication [7,8,20]. Building on these ideas new approaches to engineering Pt-rich skin/skeleton and core–shell geometries are being actively explored [1,2,8]. In addition to the prospect of enhanced catalytic performance these structures also promise considerable cost savings by maximizing Pt utilization [1,3]. In the case of Pt shell/Pt-free core particles, the usage of Pt per unit power can be reduced by a factor of 5–10 compared to Pt alloy particles [3,31]. At the same time new developments in electrode architecture remain an important area for further improvement in catalyst utilization and performance. One of the more interesting developments in the last decade has been the fabrication of nanostructured thin film (NSTF) Pt and/or Pt/TM (TM = Ni, Co, Mn, Fe) electrodes by vacuum sputter deposition [32,33]. These materials have shown 5–10 times enhanced activity toward ORR with reduced amount of Pt compared to conventional membrane electrode assembly (MEA) [32]. Furthermore the NSTF electrodes have been shown to be far more durable than carbon supported Pt particles. The combination of improvements speaks to new avenues for the design, development and utilization of electrocatalyst. Nevertheless, a cost effective means for produc-

---

[*] Corresponding author. Tel.: +1 301 975 2143; fax: +1 301 926 7679.
E-mail addresses: thomas.moffat@nist.gov, thomas.moffat@nist.gov (T.P. Moffat).

0013-4686/$ – see front matter. Published by Elsevier Ltd.
doi:10.1016/j.electacta.2010.08.013

ing compositionally tailored nanoscale electrocatalysts remains to be demonstrated.

Among the various synthetic methods being explored, electrodeposition has advantages in terms of Pt utilization and controlled mass loading since the material is deposited only on sites where both electronic and ionic contact are insured [11,14,34,35]. Recently a simple electrodeposition process for co-deposition of Pt-transition metal alloy thin films ($Pt_{1-x}M_x$, M = Ni, Co, Fe, Cu) has been studied [11,36–39]. In the case of Pt-rich alloys, co-deposition of iron-group metals proceeds by underpotential deposition (upd) concurrent with overpotential Pt deposition.

In this paper the electrodeposition of $Pt_{100-x-y}Ni_xPd_y$ thin film ternary catalysts is detailed. Potentiostatic deposition is shown to be an effective means to control the composition of the films. The electrocatalytic behavior of $Pt_{100-x-y}Ni_xPd_y$ ternary alloy films toward ORR is examined and compared to $Pt_{100-x}Ni_x$ binary and elemental Pt films produced by the same deposition method.

2. Experimental

A series of $Pt_{100-x-y}Ni_xPd_y$ ternary alloy films were electrodeposited from an electrolyte containing 0.5 mol/L NaCl, 0.1 mol/L $NiCl_2{\cdot}6H_2O$, 0.003 mol/L K_2PtCl_4, and 0.001 mol/L $PdCl_2$ at a pH of 2.5. Deposition was performed using a typical three-electrode cell with a Pt anode and saturated calomel reference electrode (SCE). Working electrodes were prepared by using electron beam evaporation to coat SiO_2/Si (1 0 0) wafers with a 3 nm Ti adhesion layer followed by a 25 nm-thick Au seed layer. The Au seeded substrates with an exposed area of 1.33 cm^2 defined by 3M plater's tape were immersed into the electrolyte for alloy deposition at room temperature. The effect of growth potential on film composition and microstructure was investigated over the range −0.1 V SCE to −0.8 V SCE. The films were grown for a fixed time of 1800 s yielding thickness values ranging from 140 nm to 600 nm. These "thick films" were used to characterize the potential dependence of the structure and composition through the use of symmetric X-ray diffraction (XRD) and energy dispersive X-ray spectroscopy (EDS). Robust compositional determination by EDS requires careful analysis because of its low analytical sensitivity [40]. In this report a ZAF (Z, atomic number; A, absorption; F, fluorescence) thin film matrix correction was used for Pt-Lα, Pd-Lα, and Ni-Kα spectra peaks collected at the accelerating voltage of 15 keV in order to avoid peak overlaps between Pt-Mα and Au-Mα lines.

The ORR kinetics for $Pt_{100-x-y}Ni_xPd_y$ ternary alloy films were examined using a Pt rotating disk electrode (RDE) with a projected area of 0.196 cm^2 as the substrate. $Pt_{100-x-y}Ni_xPd_y$ films were deposited on the Pt disk under potentiostatic conditions detailed above, although deposition was limited to 30 s giving rise to much thinner films than described in the previous paragraph. Prior to each experiment, the Pt RDE was polished using 50 nm alumina abrasive powder to remove the previously plated material. After film deposition, the RDE was rapidly removed from the chloride based plating bath and rinsed extensively with 18 MΩ cm deionized (DI) water for tens of second in an attempt to remove any residual adsorbed Cl^- from the electrode surface. This is important since halides are known to poison the ORR kinetics on Pt. The RDE was then placed in a beaker containing 100 mL DI water followed by storage in a second 100 mL beaker of DI water for transfer to the RDE set up. During mounting of the RDE the electrodeposited surface was covered with a water droplet. The electroplated surface was then immersed into an oxygen saturated 0.1 mol/L $HClO_4$ solution (Mallinckrodt Chemicals 70%)* for measuring the ORR kinetics. *(Certain trade names are mentioned for experimental information only; in no case does it imply a recommendation or endorsement by NIST). The cell contained a Pt counter electrode while the SCE reference electrode was held in an external beaker connected to the cell through a Luggin capillary to prevent contamination of the main cell by chloride crossover. Cyclic voltammetry (CV) was performed as a function of RDE rotation rate, from 400 rpm to 4900 rpm, using a sweep rate of 50 mV/s. The ORR data presented herein correspond to the positive-going potential sweep collected at room temperature. For benchmarking purposes the activity of $Pt_{100-x-y}Ni_xPd_y$ ternary alloy films was compared with Pt and $Pt_{100-x}Ni_x$ grown under the same conditions. The stated potentials are referred to the reversible hydrogen electrode (RHE) using the offset RHE = SCE + 0.304 V that was determined previously [11].

To estimate the electrochemical surface area of the electrodeposited films, CV experiments were performed from 0 V RHE to 1.0 V RHE in Ar saturated 0.1 mol/L $HClO_4$ at room temperature. The integrated H_{upd} charge between 0.040 V RHE and 0.408 V RHE was normalized to the conventional value of 0.210 mC/cm^2. The importance of area correction to conclusions regarding the intrinsic ORR kinetics cannot be overstated, and the issue remains a topic of central importance to the field. The reader is referred to the literature for a more detailed discussion of the matter [31,41,42]. In the present study the estimated area may be viewed as a conservative measure since the H_{upd} charge includes double layer capacitive effects as well as possible H absorption into the Pt–Ni–Pd thin films. The latter is expected to be less significant for dilute Pd alloys [43,44]. In addition to the magnitude of the electrode area, morphology is also expected to exert an influence on the quantification of the intrinsic ORR kinetics. When the voltammetric measurements are such that the reaction occurs under mixed control conditions it is clear that significant segments of the recessed surface area, quantified by "H_{upd}", remain largely inaccessible to O_2 thereby leading to a conservative estimate for the measured kinetics [41].

The effect of $Pt_{100-x-y}Ni_xPd_y$ dealloying during ORR measurements was quantified by examining the catalytic behavior of films as a function of as-deposited film thickness. Likewise, the evolution of the surface morphology and microstructure of $Pt_{100-x-y}Ni_xPd_y$ films was investigated by field emission scanning electron microscopy (FE-SEM) and XRD. For these experiments the "thick" $Pt_{100-x-y}Ni_xPd_y$ films grown on Au were used to ensure sufficient scattering signal.

3. Results and discussion

3.1. Characteristics of $Pt_{100-x-y}Ni_xPd_y$

X-ray diffraction patterns for $Pt_{100-x-y}Ni_xPd_y$ films electrodeposited on Au seeded Si for 1800 s at various potentials are shown in Fig. 1. The invariant Au(1 1 1) and Au(2 2 2) peaks of the gold seeded substrates are helpful as internal references for the analysis. Likewise, Pt and $Pt_{20}Ni_{80}$ films deposited at −0.6 V SCE exhibit distinct (1 1 1) peaks at about 40.11° and 42.96°, respectively. For the $Pt_{100-x-y}Ni_xPd_y$ films, the fcc (1 1 1), (2 0 0) and (2 2 2) diffraction peaks shift to higher angles as the deposition potential decreased from −0.1 V SCE to −0.8 V SCE. The (1 1 1), (2 0 0) and (2 2 2) peaks shifts for $Pt_{100-x-y}Ni_xPd_y$ films correspond to a monotonic decrease in the calculated lattice parameter from 0.3882 nm to 0.3607 nm for the (1 1 1) (and from 0.3878 nm to 0.3622 nm for the (2 0 0)) as shown in Fig. 2. The trends is congruent with increasing Ni content in the films that eventually approaches the lattice parameter of bulk fcc Ni (a_o = 0.3520 nm). The corresponding potential dependence of the ternary film compositions determined by energy dispersive X-ray spectroscopy (EDS) is shown in Fig. 3a. Five different spots were sampled on each film and the results averaged with the range indicated by the length of the data bar. The atomic concentration of Pt and Pd gradually decreased from 67% and 29% to 10% and 0.1%,

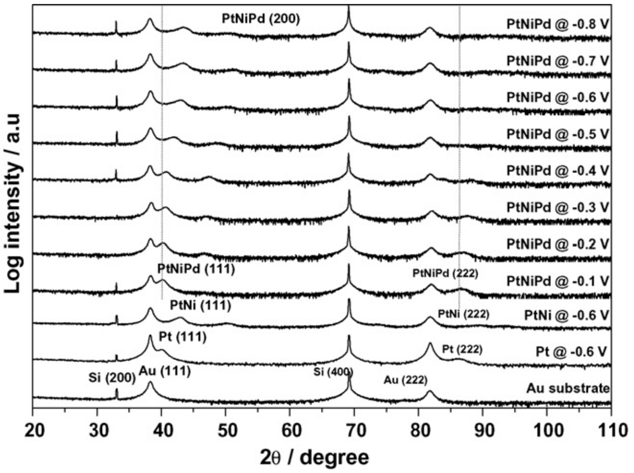

Fig. 1. X-ray diffraction patterns for a series of $Pt_{100-x-y}Ni_xPd_y$ alloy films electrodeposited for 1800 s as a function of growth potential.

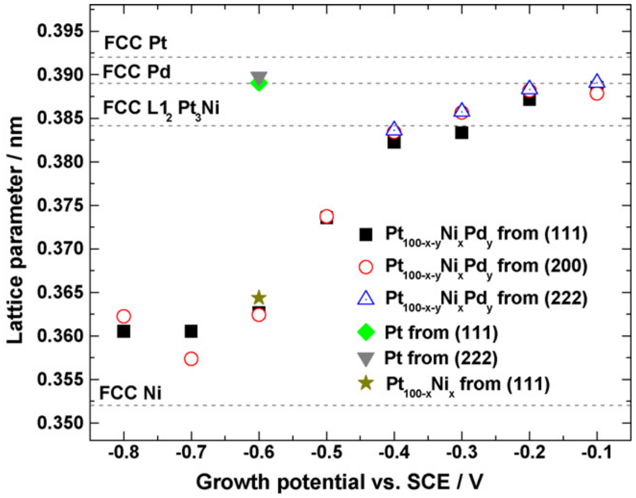

Fig. 2. Lattice constants (a_0) for electrodeposited Pt, $Pt_{100-x}Ni_x$ and $Pt_{100-x-y}Ni_xPd_y$ alloy films at various growth potentials.

respectively, while the Ni content increased from 4% to 90% as the growth potential decreased. EDS data are in good qualitative agreement with the lattice parameter change of Ni measured by XRD. Quantitative comparison would require consideration of the stress effects and a full measurement error analysis beyond the objectives of the present study. The Nernst potential for the Ni/Ni^{2+} reaction is close to −0.58 V SCE thus its co-deposition at more positive potentials occurs by an underpotential process. In contrast both Pd and Pt deposition occur at overpotentials. If Pt and Pd deposition occur under mass transport limited conditions the ratio in the deposit should reflect that of the electrolyte, namely 3:1 Pt:Pd. This is the case for film deposited at −0.2 V SCE, −0.3 V SCE and −0.4 V SCE. At −0.1 V SCE the ratio is slightly less and may reflect some kinetic restraint on the Pt half reaction relative to Pd. The ratio increases significantly to a factor in excess of 10 at potentials below −0.5 V SCE. Importantly, the reversible potential for proton reduction is −0.389 V SCE and both Pt^{2+} and Pd^{2+} species are subject to reduction by the parasitic hydrogen produced at more negative potential. For pH 2.5, diffusion limited proton reduction (3.2 mmol/L H_3O^+) would yield an upper bound for the interface H_2 concentration of 1.6 mmol/L. The relative concentration of the reactive species, 3 mmol/L Pt^{2+}, 1 mmol/L Pd^{2+} and 1.6 mmol/L H_2 and prior reports that the kinetics of Pd reduction tends to be faster than that of Pt

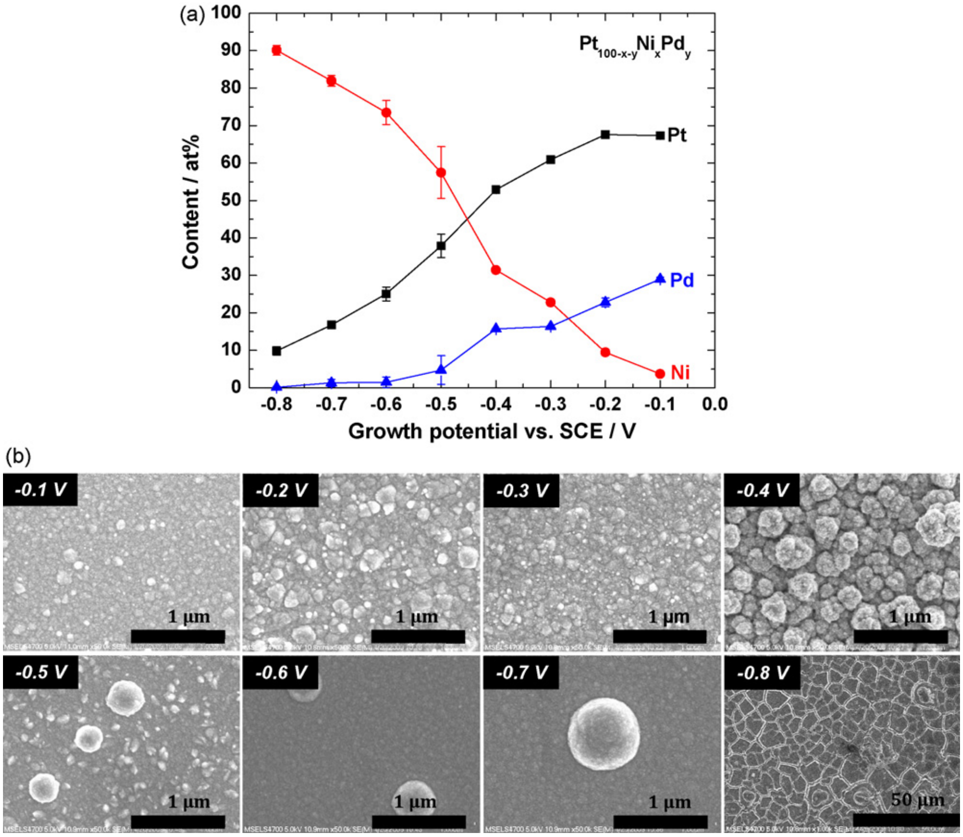

Fig. 3. (a) Compositional analyses by EDS and (b) FE-SEM images for $Pt_{100-x-y}Ni_xPd_y$ alloy films electrodeposited for 1800 s as a function of growth potential.

Table 1
Grain size and film thickness of the $Pt_{100-x-y}Ni_xPd_y$ films grown on Au seeded substrate at various potential for 1800 s.

Growth potential (V) SCE	Grain size from 1 1 1 peak (nm)	Film thickness (nm)
$Pt_{100-x-y}Ni_xPd_y$ at −0.1 V	10.99	260 ± 1.0
$Pt_{100-x-y}Ni_xPd_y$ at −0.2 V	10.54	320 ± 11.0
$Pt_{100-x-y}Ni_xPd_y$ at −0.3 V	9.80	410 ± 13.4
$Pt_{100-x-y}Ni_xPd_y$ at −0.4 V	9.62	590 ± 77.6
$Pt_{100-x-y}Ni_xPd_y$ at −0.5 V	8.25	140 ± 7.1
$Pt_{100-x-y}Ni_xPd_y$ at −0.6 V	7.77	210 ± 8.4
$Pt_{100-x-y}Ni_xPd_y$ at −0.7 V	7.29	500 ± 5.5
$Pt_{100-x-y}Ni_xPd_y$ at −0.8 V	6.54	Peeled off

[45,46] may account for the selective fall off in Pd incorporated in the alloy deposit grown at potentials below −0.5 V SCE. This explanation is congruent with the surface morphologies observed by SEM where, as shown in Fig. 3b, a limited volume fraction of large spherical particle precipitates are evident in films grown between −0.5 V SCE and −0.7 V SCE. Qualitative EDS indicates a high concentration of Pd in these particles compared to the neighboring surface.

Furthermore, the corresponding film thickness measured by FE-SEM examination of cleaved cross-sections reveals a distinct transition in the same potential regime. As shown in Table 1 for a fixed deposition time, the film thickness increased from 260 nm to 590 nm as the growth potential decreased from −0.1 V SCE to −0.4 V SCE. At −0.5 V SCE the thickness suddenly dropped to 140 nm at −0.5 V SCE. The thickness increased again to 500 nm at −0.7 V SCE. The film deposited at −0.8 V SCE was found to exhibit a mud crack surface pattern, with typical crack separation distance of 5 μm. During cross-sectioning the film spalled from the substrate preventing an accurate determination of its thickness.

The width of the (1 1 1) diffraction peak was used to estimate grain size of the films using the Scherrer equation. As shown in Table 1 the grain size decreased monotonically from 11 nm to 6 nm as the growth potential decreased from −0.1 V SCE to −0.8 V SCE.

3.2. *ORR studies on $Pt_{100-x-y}Ni_xPd_y$*

The kinetics of the ORR on $Pt_{100-x-y}Ni_xPd_y$ films were examined using a RDE. In contrast to the “thick” films used for structural and compositional evaluation, “thin” films were grown on the Pt RDE for 30 s at the specified potentials. Prior work with Pt alloy co-deposition indicates that there is little change in film composition with thickness [35,36] so that the relationship between structure and composition established with the “thick films” can be applied to the “thin films”. Prior to measuring the ORR kinetics, the electroactive surface area of the deposited films was assayed by voltammetrically measuring the H_{upd} charge in Ar saturated 0.1 mol/L $HClO_4$. Quasi steady-state voltammograms for the $Pt_{100-x-y}Ni_xPd_y$ alloy films are shown in Fig. 4a. The average charge measured for the anodic and cathodic waves between 0.039 V RHE and 0.408 V RHE is given in Table 2. Interestingly the H_{upd} charge tends to increase with the as-desposited Ni content in the films although the trend is not monotonic. For example, the H_{upd} charge for the film grown at −0.6 V SCE is less than that for the more Pt-Pd rich films grown −0.3 V SCE. Although surface roughness is expected to increase with as-deposited Ni content due to subsequent dealloying, the as-deposited film thickness might be less due to the parasitic effects of proton reduction alluded to early. Pd additions may also lead to contributions arising from hydrogen absorption and thereby an overestimate of the electroactive area. In the first approximation the H_{upd} charge for the $Pt_{100-x-y}Ni_xPd_y$ films was normalized by 210 $\mu C/cm^2$; the commonly accepted value for a monolayer charge of adsorbed hydrogen on polycrystalline Pt [47].

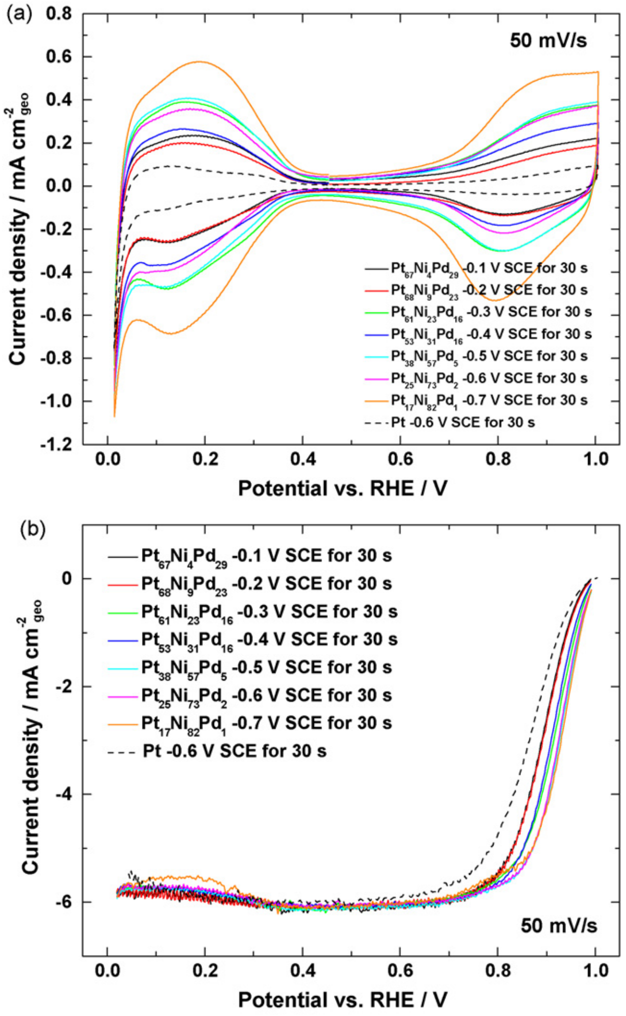

Fig. 4. (a) Cyclic voltammetries in Ar saturated 0.1 mol/L $HClO_4$ and (b) RDE measurements for ORR in O_2 saturated 0.1 mol/L $HClO_4$ with 1600 rpm on a series of $Pt_{100-x-y}Ni_xPd_y$ films grown for 30 s.

Following saturation of the electrolyte with O_2 the positive-going voltammetric curves for ORR on a series of $Pt_{100-x-y}Ni_xPd_y$ thin films were collected using a RDE and normalized by the geometrically projected area (0.196 cm^2). The ORR kinetics on the $Pt_{100-x-y}Ni_xPd_y$ alloy films exhibit half-wave potentials ($E_{1/2}$) that are 26–65 mV greater than that of pure Pt grown at −0.6 V SCE as shown in Fig. 4b. A diffusion limited current density of ~6 mA/cm^2 is observed below 0.7 V RHE followed by slight decrease below 0.3 V RHE due to contributions from the anodic oxidation of H_{upd}. The mass transfer corrected kinetics can be obtained using the Levich–Koutecky equation where $i_{kinetic}$ is the kinetic current at a given potential and $i_{limited}$ is the limiting current.

$$\frac{1}{i_{measured}} = \frac{1}{i_{kinetic}} + \frac{1}{i_{limited}} \qquad (1)$$

Graphically, the slope of the inverse of the measured current versus the square root of the reciprocal of the RDE rotation rate (not shown) is congruent with diffusion limited $4e^-$ reduction of O_2 to H_2O consistent with other work on Pt and Pt alloys [48,49]. The mass transport corrected ORR kinetics for each alloy at 0.9 V RHE is summarized in Table 2. Compared to electrodeposited Pt the apparent ORR kinetics for the alloys are substantially greater, in some cases as much as a factor of 6–8 times. However consideration of the H_{upd} charge suggests that much of this increase is due to expansion of the electroactive area that accompanies Ni dealloying. As shown

Table 2
ORR kinetics at 0.9 V RHE as a function of growth potentials (the films were grown for 30 s at each growth potential).

Growth potential (V) SCE	$i_{\text{kinetic, geo}}$ (mA/cm^2)	H_{upd} charge (mC/cm^2)	H_{upd} area (cm^2)	$i_{\text{kinetic, }H_{\text{upd}}}$ (mA/cm^2)
Pt at −0.3 V	3.23	1.50	7.13	0.45
Pt at −0.6 V	1.58	0.48	2.26	0.7
$Pt_{100-x-y}Ni_xPd_y$ at −0.10 V	2.98	1.20	5.73	0.52
$Pt_{100-x-y}Ni_xPd_y$ at −0.20 V	3.2	1.09	5.18	0.62
$Pt_{100-x-y}Ni_xPd_y$ at −0.30 V	6.84	2.11	10.07	0.68
$Pt_{100-x-y}Ni_xPd_y$ at −0.35 V	5.39	1.45	6.89	0.78
$Pt_{100-x-y}Ni_xPd_y$ at −0.40 V	5.31	1.58	7.50	0.71
$Pt_{100-x-y}Ni_xPd_y$ at −0.45 V	6.22	1.42	6.78	0.92
$Pt_{100-x-y}Ni_xPd_y$ at −0.50 V	9.81	2.10	10.01	0.98
$Pt_{100-x-y}Ni_xPd_y$ at −0.55 V	7.79	1.68	8.01	0.97
$Pt_{100-x-y}Ni_xPd_y$ at −0.60 V	10.14	1.81	8.63	1.18
$Pt_{100-x-y}Ni_xPd_y$ at −0.65 V	5.02	2.11	10.03	0.50
$Pt_{100-x-y}Ni_xPd_y$ at −0.70 V	13.31	3.0	14.68	0.91

in Table 2, H_{upd} normalization results in the ORR kinetics increasing as the growth potential is made more negative. The maximum area corrected ORR enhancement factor is reduced to a factor of 1.7 times Pt for the $Pt_{25}Ni_{73}Pd_2$ film grown at −0.6 V SCE.

A more detailed comparison of the ORR behavior of $Pt_{57}Ni_{27}Pd_{16}$ film grown at −0.35 V SCE (a Pt_3Ni analog) to that of Pt grown at a similar potential, −0.3 V SCE, is given in Fig. 5. Since the Pt deposition reaction proceeds at the diffusion limit the total Pt mass loading for both films is identical, the alloy film only being thicker due to co-deposition of Ni and Pd. Voltammetry in the absence of O_2 reveals practically identical H_{upd} charge and, by inference, a similar electroactive area. Subsequent ORR measurements reveal the enhanced activity of the alloy. The kinetic enhancement factor at 0.9 V RHE is on the order of 1.7 as shown in Fig. 5c and d. This is slightly less than the factor of 2.5 observed for binary $Pt_{72}Ni_{28}$ films produced by the same means [11].

The influence of dealloying-derived area expansion on the ORR kinetics was examined for a series of alloy films grown to different thicknesses at −0.6 V SCE. The H_{upd} electroactive area of each was determined prior to ORR measurements. The half-wave potential of the ORR response exhibits a monotonic shift with the as-deposited film thickness as shown in Fig. 6a. A complication is clearly evident for the thickest films where the shape of the curve deviates sharply at 0.9 V RHE presumably due to some complex hydrodynamic interactions between the thick dealloyed material and the electrolyte. The Levich equation was used

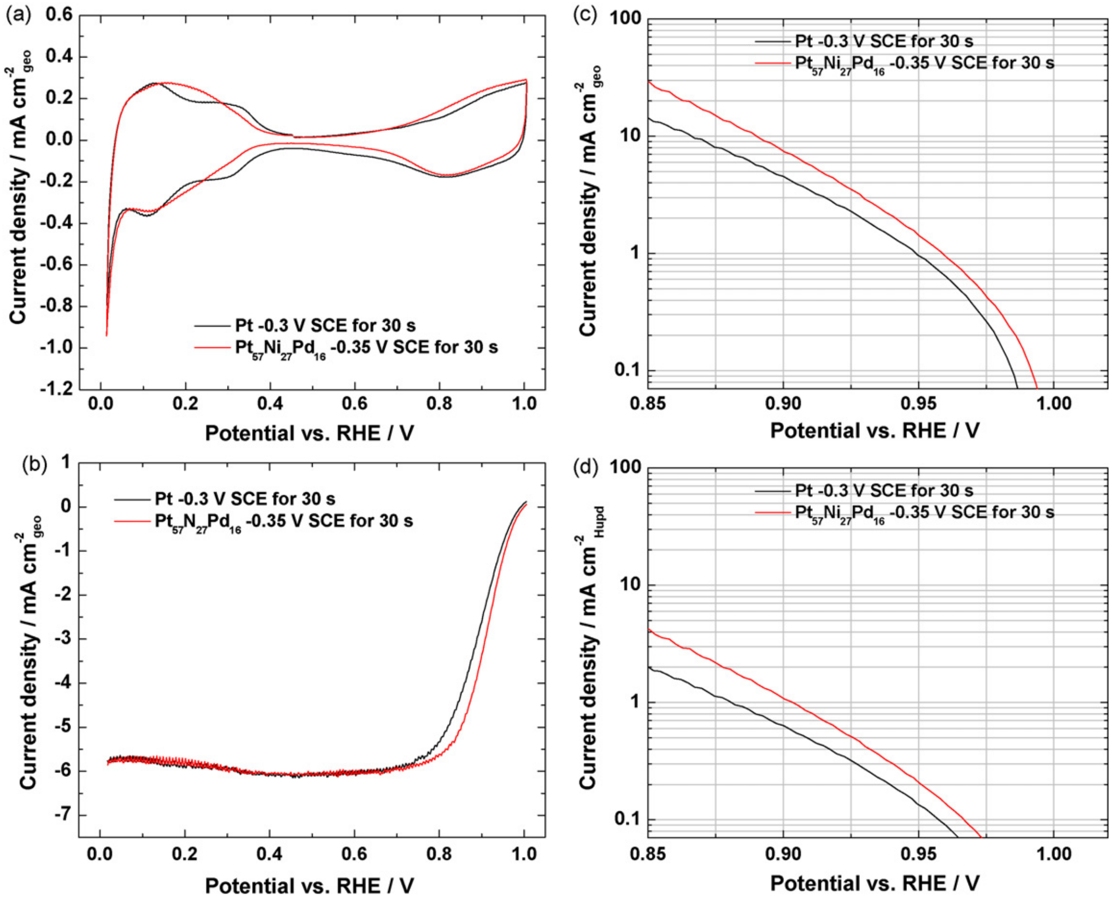

Fig. 5. (a) Cyclic voltammetries in Ar saturated 0.1 mol/L $HClO_4$ on Pt and $Pt_{57}Ni_{27}Pd_{16}$ films grown at −0.3 V SCE and −0.35 V SCE for 30 s, (b) RDE measurements, (c) mass transport corrected Tafel plot, and (d) H_{upd} area corrected Tafel plot for ORR in O_2 saturated 0.1 mol/L $HClO_4$ with 1600 rpm on Pt and $Pt_{57}Ni_{27}Pd_{16}$ films grown at −0.3 V SCE and −0.35 V SCE for 30 s.

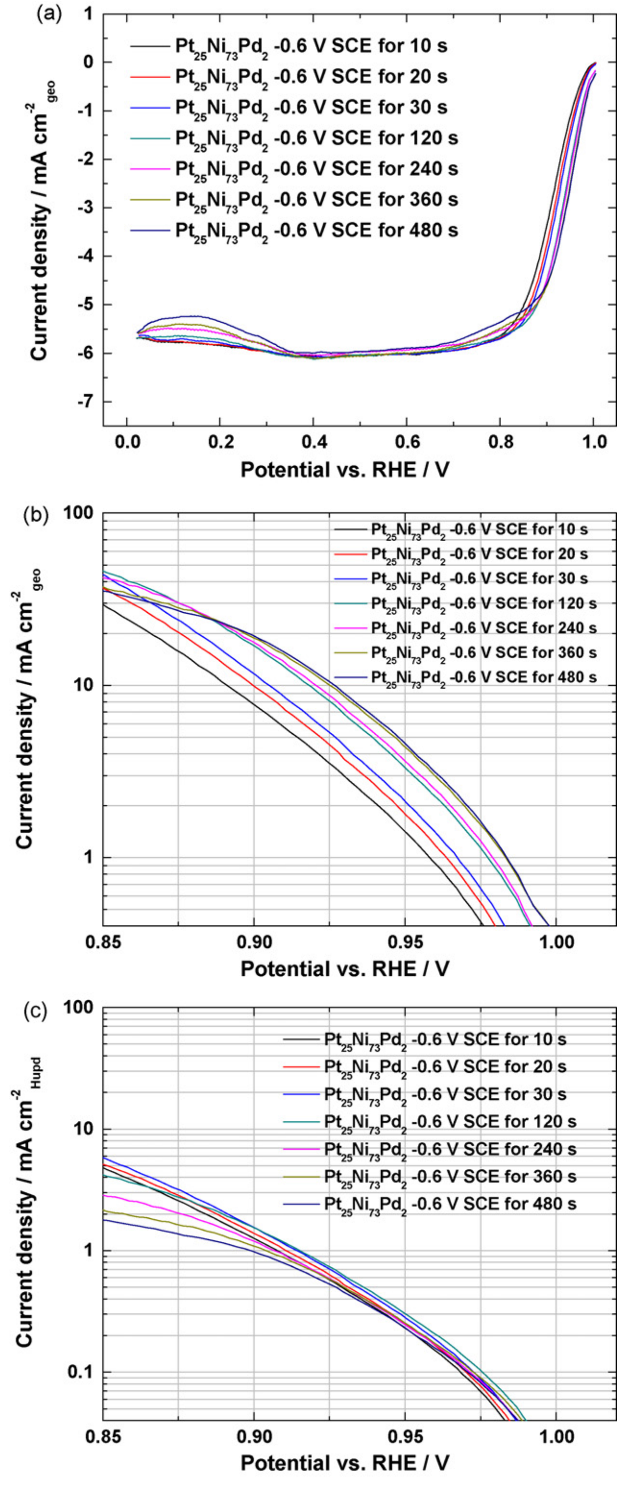

Fig. 6. (a) RDE measurements, (b) mass transport corrected Tafel plot, and (c) H_{upd} area corrected Tafel plot for the ORR in O_2 saturated 0.1 mol/L $HClO_4$ with 1600 rpm on $Pt_{25}Ni_{73}Pd_2$ films grown at −0.6 V SCE as a function of growth time.

to isolate the kinetic contribution and, as shown in Fig. 6b, the mass transport corrected ORR kinetics ($i_{kinetic,\,geo}$ at 0.9 V RHE) increased monotonically from 7.5 mA/cm^2 to 15 mA/cm^2 as the film growth time increased from 10 s to 120 s. Thereafter the ORR kinetics scatter between 15 mA/cm^2 and 20 mA/cm^2. The corresponding H_{upd} normalized ORR kinetics ($i_{kinetic,\,H_{upd}}$) are shown in Fig. 6c with a maximum activity observed for the film grown for 120 s followed by decreasing performance for the thicker films. The apparent loss for the thicker films may be attributed to the inability of O_2 to access the recessed dealloyed regions that are assayed by the H_{upd} measurements. The effect is particularly accentuated at potentials at or below the half-wave potential where a substantial O_2 depletion gradient exists in the interfacial region. A more suitable measurement of the intrinsic activity of the thicker dealloyed layer is obtained at smaller overpotentials where convolution of the O_2 depletion with the porous electrode is less severe.

3.3. Comparison of ORR on $Pt_{100-x-y}Ni_xPd_y$ and $Pt_{100-x}Ni_x$

The ORR electrocatalytic activity of $Pt_{25}Ni_{73}Pd_2$ was evaluated by comparing it with $Pt_{20}Ni_{80}$ and Pt films electrodeposited under similar conditions. Electrodeposited Ni-rich $Pt_{100-x}Ni_x$ alloy films ($x = \sim 80\%$) have been reported to exhibit 4-fold higher, H_{upd} area corrected ORR kinetics compared to pure Pt films. For this study Pt, $Pt_{20}Ni_{80}$, and $Pt_{25}Ni_{73}Pd_2$ films were deposited on a Pt RDE at −0.6 V SCE for 30 s. For all three samples Pt deposition occurs under transport limited conditions thereby resulting in the same Pt mass loading for a given deposition time. Subsequent Ni dealloying during voltammetric cycling in 0.1 mol/L $HClO_4$ leads to area expansion as reflected by changes in the H_{upd} with cycling. The steady-state voltammogram for the three materials in Ar saturated 0.1 mol/L $HClO_4$ are shown in Fig. 7a. The shape of the H_{upd} region is notably different for the Pd alloy and may reflect a contribution from H absorption. Comparison of the expansion in charge associated with the oxide formation and reduction suggests that area change in the H_{upd} region is still dominated by hydrogen adsorption versus absorption as has been reported for Pt-rich Pt–Pd alloys [43,44]. Measurement of the ORR, shown in Fig. 7b, reveals a positive shift in the half-wave potential for $Pt_{25}Ni_{73}Pd_2$ and $Pt_{20}Ni_{80}$, relative to Pt. The respective shifts of 61 mV and 66 mV translate to an increase in the mass transport corrected rate constant ($i_{kinetic,\,geo}$) by a factor of 5 and 6, respectively, when evaluated at 0.9 V RHE as summarized in Table 3. Thus, for a fixed Pt loading, formation and subsequent dealloying of the thin alloy films yields an increase in the ORR Pt mass activity that is more than a factor of 5. The area normalized ORR reactivity, based on the H_{upd} charge, reduces this to a factor of 1.4 and 2.3, respectively. Mass transport corrected Tafel plots for the three specimens with fixed Pt loading are given in Fig. 7c while the H_{upd} area corrected versions are shown in Fig. 7d. Clearly, the enhanced ORR kinetics for the alloys arise from a combination of enhanced electrocatalysis and area expansion due to dealloying. The area normalized result indicates that the intrinsic ORR reactivity spans a range of 0.7–1.7 depending on the alloy composition and potential.

3.4. Stability of $Pt_{20}Ni_{80}$ and $Pt_{25}Ni_{73}Pd_2$

The dealloying of electrodeposited $Pt_{25}Ni_{73}Pd_2$ and $Pt_{20}Ni_{80}$ was evaluated by monitoring changes in the cyclic voltammetric behavior in Ar saturated 0.1 mol/L $HClO_4$. At the same time X-ray diffraction was used to characterize the resulting structural evolution of the films. The “thick” electrodeposited films (>100 nm) grown for 1800 s on Au substrates were used to ensure strong X-ray scattering power for the conventional laboratory diffraction experiment.

As shown in Fig. 8a, the initial cyclic voltammogram for $Pt_{25}Ni_{73}Pd_2$ reveals a potential independent current associated with the growth, dissolution and capacitance of the passive nickel oxide film. Previous work indicated that cycling the potential into the H_{upd} region enables activation of Ni dissolution in 0.1 mol/L $HClO_4$ with significant dealloying occurring with continued cycling [32,50]. The voltammetric characteristics of H_{upd} and oxide formation and reduction on Pt become increasingly evident. The

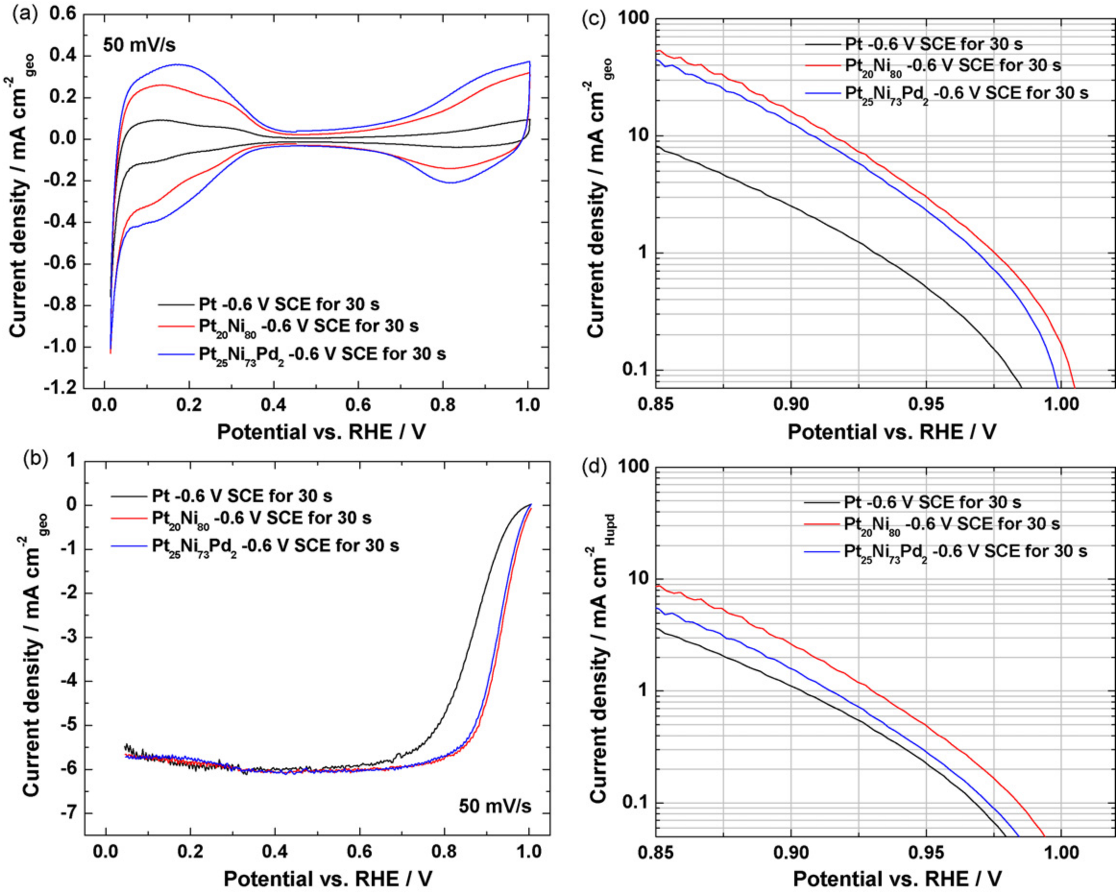

Fig. 7. (a) Cyclic voltammetries in Ar saturated 0.1 mol/L $HClO_4$ on electrodeposited Pt, $Pt_{20}Ni_{80}$, and $Pt_{25}Ni_{73}Pd_2$ films, (b) positive-going polarization curves, (c) mass transport corrected Tafel plot, and (d) H_{upd} area corrected Tafel plot for the ORR in O_2 saturated 0.1 mol/L $HClO_4$ with 1600 rpm on electrodeposited Pt, $Pt_{20}Ni_{80}$, and $Pt_{25}Ni_{73}Pd_2$ films.

magnitude of the H_{upd} wave for $Pt_{25}Ni_{73}Pd_2$ increases, passing through a maximum around 20 cycles before settling towards a quasi steady-state result that reflects the behavior of Pt. FE-SEM images of the film surface before and after cycling are shown in Fig. 8b and c, and Ni dealloying is clearly evident by the formation of cracks and very fine scale porosity. Cross-sections of the film reveal dealloying leads to decrease in film thickness from 210 nm to 100 nm. X-ray diffraction shown in Fig. 8d reveals a shift in the position of the 1 1 1 and 2 0 0 peaks to lower angles, from 43.59° to 41.05° for the 1 1 1 and from 50.88° to 47.65° for the 2 0 0. Comparison to the 1 1 1 peak position for pure Pt grown under similar conditions indicates that significant Ni remains within the dealloyed $Pt_{25}Ni_{73}Pd_2$ film. This was qualitatively confirmed by EDS measurements of the porous dealloyed layer. The lattice parameter shift from 0.3593 nm to 0.3805 nm for the (1 1 1) suggests that the dealloyed reminant has a composition close to $Pt_{70}Ni_{30}$ stoichiometry.

Consistent with a previous study [11] similar trends were observed for a $Pt_{20}Ni_{80}$ film although interestingly the area expansion accompanying dealloying was more substantial (4×) than for the Pd containing alloy as revealed by comparing the H_{upd} and Pt oxidation and reduction waves in Fig. 9a compared to Fig. 8a. SEM examination of the cross-section reveals a decrease in the film thickness from 446 nm to 358 nm upon dealloying. The more substantial area increase might be associated with the thicker film observed for the Pt–Ni system 446 nm relative to the Pt–Ni–Pd films (210 nm) grown at this potential. The more extensive dealloying of $Pt_{20}Ni_{80}$ compared to $Pt_{25}Ni_{73}Pd_2$ may also be ascribed to the lower combined Pt–Pd content, 20% versus 27%, in the as-deposited alloy. For the magnifications examined, the FE-SEM images of the as-deposited (Fig. 9b) and dealloyed (Fig. 9c) material were effectively indistinguishable from those for $Pt_{25}Ni_{73}Pd_2$. X-ray diffraction shown in Fig. 9d reveals a shift in the position of the 1 1 1 peak from 42.89° to 41.20° while the 2 0 0 shifts from

Table 3
Comparison of ORR kinetics at 0.9 V RHE and 0.95 V RHE on $Pt_{25}Ni_{73}Pd_2$, $Pt_{20}Ni_{80}$, and Pt films electrodeposited at −0.6 V SCE.

Materials	$i_{kinetic,\,geo}$ at 0.9 V RHE (mA/cm^2)	H_{upd} charge (mC/cm^2)	H_{upd} area (cm^2)	$i_{kinetic,\,H_{upd}}$ at 0.9 V RHE (mA/cm^2)
Pt	2.43	0.48	2.26	1.07
$Pt_{20}Ni_{80}$	15.04	1.29	6.14	2.45
$Pt_{25}Ni_{73}Pd_2$	12.33	1.70	8.08	1.53

Materials	$i_{kinetic,\,geo}$ at 0.95 V RHE (mA/cm^2)	H_{upd} charge (mC/cm^2)	H_{upd} area (cm^2)	$i_{kinetic,\,H_{upd}}$ at 0.95 V RHE (mA/cm^2)
Pt	0.48	0.48	2.26	0.21
$Pt_{20}Ni_{80}$	2.76	1.29	6.14	0.45
$Pt_{25}Ni_{73}Pd_2$	2.18	1.70	8.08	0.27

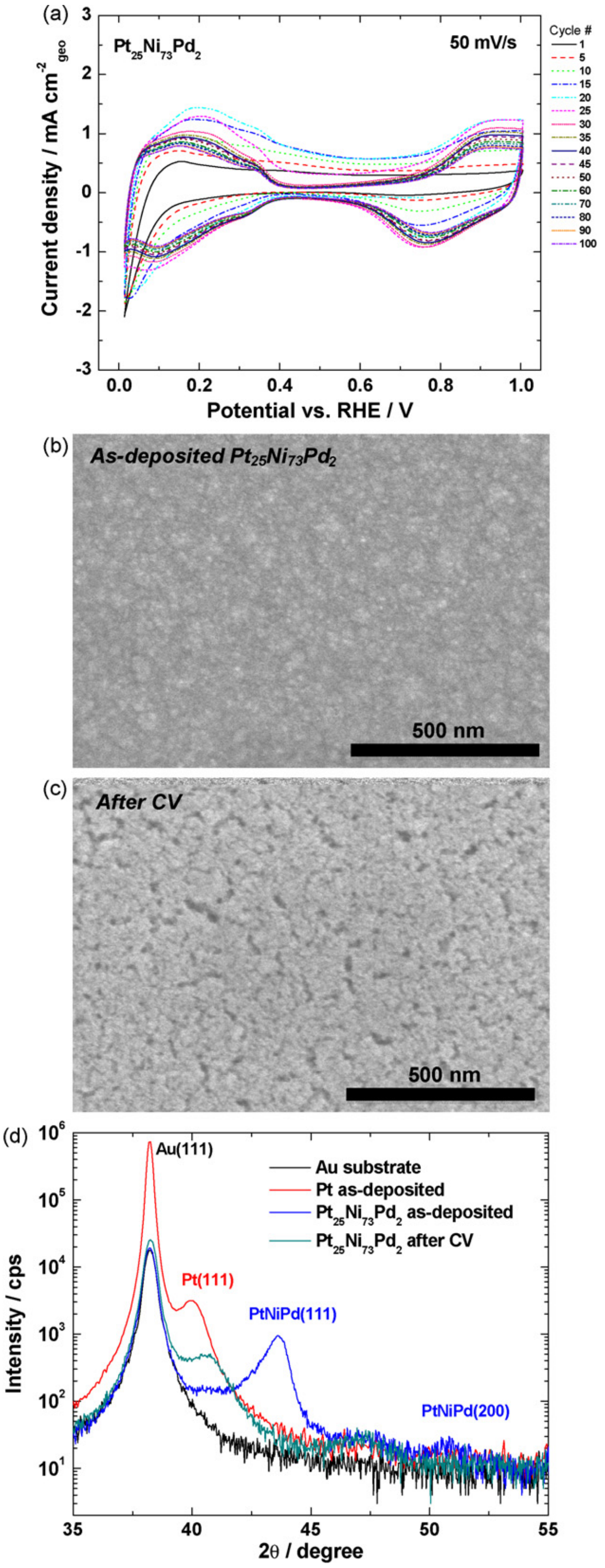

Fig. 8. (a) Multicyclic voltammogram for $Pt_{25}Ni_{73}Pd_2$ films grown for 1800 s at −0.6 V SCE, FE-SEM images of $Pt_{25}Ni_{73}Pd_2$ film (b) as-deposited, (c) after CVs, and (d) X-ray diffraction patterns of $Pt_{25}Ni_{73}Pd_2$ film before and after CVs in Ar saturated 0.1 mol/L $HClO_4$.

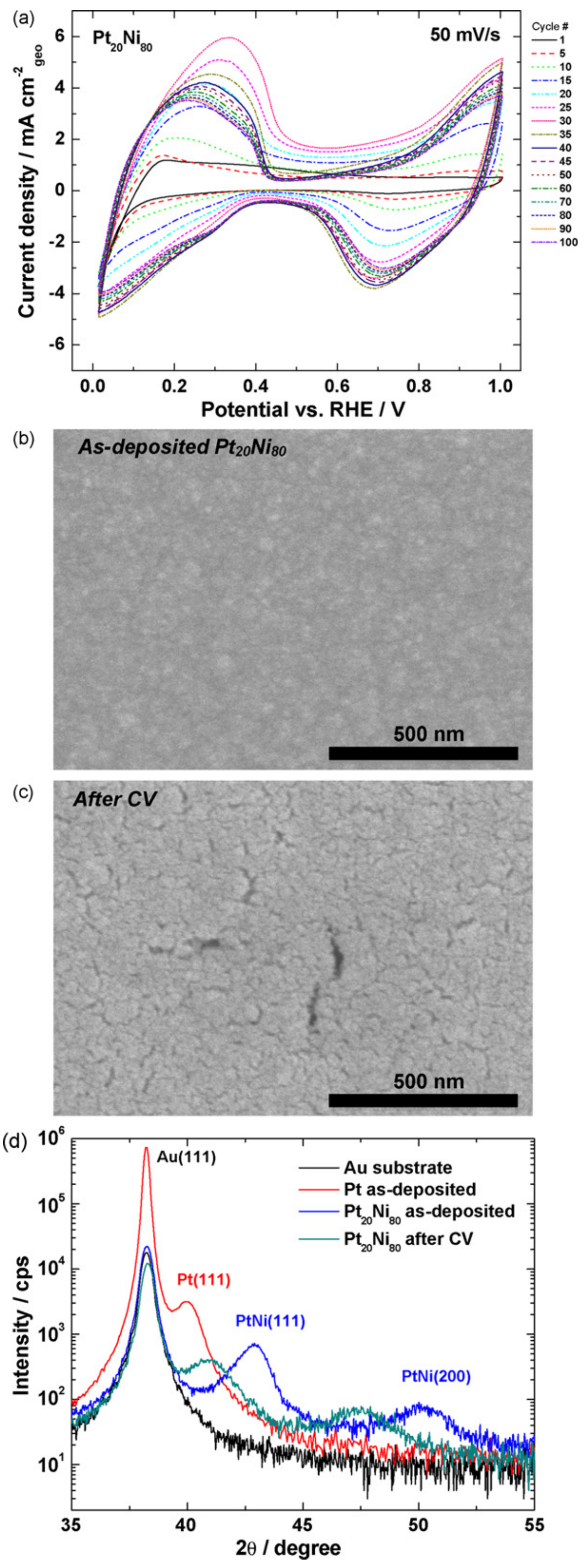

Fig. 9. (a) Multicyclic voltammogram for $Pt_{20}Ni_{80}$ films grown for 1800 s at −0.6 V SCE, FE-SEM images of $Pt_{20}Ni_{80}$ film (b) as-deposited, (c) after CVs, and (d) X-ray diffraction patterns of $Pt_{20}Ni_{80}$ films before and after CVs in Ar saturated 0.1 mol/L $HClO_4$.

50.20° to 47.54°. This corresponds to a change in the lattice parameter from 0.3649 nm to 0.3792 nm for the 1 1 1 plane spacing and from 0.3632 nm to 0.3822 nm for the 2 0 0. Comparison with lattice parameter data for electrodeposited Pt–Ni films [37] indicates the dealloyed electrode has a composition close to $Pt_{65}Ni_{35}$.

Ni-rich Pt–(Pd)–Ni alloys show significant Ni dealloying during extended voltammetric cycling at room temperature. However the dealloying appears to be limited by a threshold that likely represents a convolution of kinetic (surface diffusion) and geometric (i.e. percolation) factors [51,52] associated with an average alloy composition in the range $Pt_{70}Ni_{30}$ as determined by a Vegard's law approximation. The actual composition of the dealloyed materials is probably slightly different due to capillarity and related stress effects associated with dealloying and the remnant material.

4. Conclusions

The kinetics of the ORR were measured on a series of electrodeposited $Pt_{100-x-y}Ni_xPd_y$ films. The alloys were produced by an electrodeposition process that involved a combination of underpotential and overpotential reactions. For Pt-rich $Pt_{100-x-y}Ni_xPd_y$ alloy films ($x < 0.65$) Ni co-deposition occurred at underpotentials while for Ni-rich films ($x > 0.65$) the deposition proceeded at overpotentials. Potentiostatic deposition enables control of the alloy composition that is a monotonic function of the growth potential. For thin film with fixed Pt loading the $Pt_{25}Ni_{73}Pd_2$ and $Pt_{20}Ni_{80}$ alloys exhibit a 5–6-fold enhancement of the mass transport corrected ORR kinetics. However, based on H_{upd} measurements a significant portion of this is associated with surface area expansion that accompanies partial dealloying of Ni. Using H_{upd} to correct for the electroactive area indicate that the $Pt_{25}Ni_{73}Pd_2$ and $Pt_{20}Ni_{80}$ alloys have an intrinsic activity toward ORR at 0.9 V RHE that is 1.4 and 2.3-fold greater, respectively, than Pt.

References

[1] R.R. Adzic, J. Zhnag, K. Sasaki, M.B. Vukmirovic, M. Shao, J.X. Wang, A.U. Nilekar, M. Mavrikakis, J.A. Valerio, F. Uribe, Top. Catal. 46 (2007) 249.
[2] A.U. Nilekar, Y. Xu, J.L. Zhang, M.B. Vukmirovic, K. Sasaki, R.R. Adzic, M. Mavrikakis, Top. Catal. 46 (2007) 276.
[3] J. Zhang, F.H.B. Lima, M. Shao, K. Sasaki, J.X. Wnag, J. Hanson, R.R. Adzic, J. Phys. Chem. B 109 (2005) 22701.
[4] L. Xiong, A. Manthiram, J. Electrochem. Soc. 152 (2005) A697.
[5] T. Toda, H. Igarashi, H. Uchida, M. Watanabe, J. Electrochem. Soc. 146 (1999) 3750.
[6] V.R. Stamenkovic, B. Fowler, B.S. Mun, G.F. Wang, P.N. Ross, C.A. Lucas, N.M. Markovic, Science 315 (2007) 493.
[7] V.R. Stamenkovic, B.S. Mun, K.J.J. Mayrhofer, P.N. Ross, N.M. Markovic, J. Rossmeisl, J. Greeley, J. Nørskov, Angew. Chem. Int. Ed. 45 (2006) 2897.
[8] V.R. Stamenkovic, B.S. Mun, M. Arenz, K.J.J. Mayrhofer, C.A. Lucas, G.F. Wang, P.N. Ross, N.M. Markovic, Nat. Mater. 6 (2007) 241.
[9] P. Mani, P. Srivastava, P. Strasser, J. Phys. Chem. C 112 (2008) 2770.
[10] P. Strasser, S. Koh, J. Greeley, Phys. Chem. Chem. Phys. 10 (2008) 3670.
[11] T.P. Moffat, J.J. Mallett, S.-M. Hwang, J. Electrochem. Soc. 156 (2009) B238.
[12] S. Mukerjee, S. Srinivasan, J. Electroanal. Chem. 357 (1993) 201.
[13] U.A. Paulus, A. Wokaun, G.G. Scherer, T.J. Schmidt, V. Stamenkovic, N.M. Markovic, P.N. Ross, Electrochim. Acta 47 (2002) 3787.
[14] K. Jayasayee, V.A. Dam, T. Verhoeven, S. Celebi, F.A. de Bruijn, J. Phys. Chem. C 113 (2009) 20371.
[15] F.H.B. Lima, J.R.C. Salgado, E.R. Gonzalez, E.A. Ticianelli, J. Electrochem. Soc. 154 (2007) A369.
[16] A. Seo, J. Lee, K. Han, H. Kim, Electrochim. Acta 52 (2006) 1603.
[17] J.F. Whitacre, T.I. Valdez, S.R. Narayanan, Electrochim. Acta 53 (2008) 3680.
[18] A. Bonakdarpour, K. Stevens, G.D. Vernstrom, R. Atanasoski, A.K. Schmoeckel, M.K. Debe, J.R. Dahn, Electrochim. Acta 53 (2007) 688.
[19] J.H. Cho, W.J. Roh, D.K. Kim, J.B. Yoon, J.H. Choy, H.S. Kim, J. Chem. Soc., Faraday Trans. 94 (1998) 2835.
[20] G.E. Ramirez-Caballero, Y. Ma, R. Callejas-Tovar, P.B. Balbuena, Phys. Chem. Chem. Phys. 12 (2010) 2209.
[21] E. Antolini, Energy Environ. Sci. 2 (2009) 915.
[22] M.H. Shao, K. Sasaki, P. Liu, R.R. Adzic, Z. Phys. Chem. 221 (2007) 1175.
[23] B. Lim, M.J. Jiang, P.H.C. Camargo, E.C. Cho, J. Tao, X.M. Lu, Y.M. Zhu, Y.A. Xia, Science 324 (2009) 1302.
[24] G. Ramos-Sanchez, H. Yee-Madeira, O. Solorza-Feria, Int. J. Hydrogen Energy 33 (2008) 3596.
[25] X.P. Wang, N. Kariuki, J.T. Vaughey, J. Goodpaster, R. Kumar, D.J. Myers, J. Electrochem. Soc. 155 (2008) B602.
[26] W.M. Wang, D. Zheng, C. Du, Z.Q. Zou, X.G. Zhang, B.J. Xia, H. Yang, D.L. Akins, J. Power Sources 167 (2007) 243.
[27] J. Kim, T. Momma, T. Osaka, J. Power Sources 189 (2009) 909.
[28] S. Guerin, B.E. Hayden, C.E. Lee, C. Mormiche, A.E. Russell, J. Phys. Chem. B 110 (2006) 14355.
[29] R. Wang, H. Li, S. Ji, H. Wang, Z. Lei, Electrochim. Acta 55 (2010) 1519.
[30] M.T. Paffett, J.G. Beery, S. Gottesfeld, J. Electrochem. Soc. 135 (1988) 1431.
[31] S. Gottesfeld, in: M.T.M. Koper (Ed.), Fuel Cell Catalysis, John Wiley & Sons, 2009 (Chapter 1).
[32] M.K. Debe, A.K. Schmoeckel, G.D. Vernstrorn, R. Atanasoski, J. Power Sources 161 (2006) 1002.
[33] J.H. Wee, K.Y. Lee, S.H. Kim, J. Power Sources 165 (2007) 667.
[34] E.J. Taylor, E.B. Anderson, N.R.K. Vilambi, J. Electrochem. Soc. 139 (1992) L45.
[35] S.M. Ayyadurai, Y.-S. Choi, P. Ganesan, S.P. Kumaraguru, B. Popov, J. Electrochem. Soc. 154 (2007) B1063.
[36] J.J. Mallett, U. Bertocci, J.E. Bonevich, T.P. Moffat, J. Electrochem. Soc. 156 (2009) D531.
[37] J.J. Mallett, E.B. Svedberg, J.E. Bonevich, A.J. Shapiro, W.F. Egelhoff, T.P. Moffat, J. Electrochem. Soc. 155 (2008) D1.
[38] J.J. Mallett, E.B. Svedberg, S. Sayan, A.J. Shapiro, L. Wielunski, T.E. Madey, P.J. Chen, W.F. Egelhoff, T.P. Moffat, Electrochem. Solid-State Lett. 8 (2005) C15.
[39] J.J. Mallett, E.B. Svedberg, S. Sayan, A.J. Shapiro, L. Wielunski, T.E. Madey, W.F. Egelhoff, T.P. Moffat, Electrochem. Solid-State Lett. 7 (2004) C121.
[40] Z. Samardžija, RožmanF K.Ž., S. Kobe, Mater. Charact. 60 (2009) 1241.
[41] K.J.J. Mayrhofer, D. Strmcnik, B.B. Blizanac, V. Stamenkovic, M. Arenz, N.M. Markovic, Electrochim. Acta 53 (2008) 3181.
[42] Y. Liu, S. Bliznakov, N. Dimitrov, J. Phys. Chem. C 113 (2009) 12362.
[43] M. Grden, A. Czerwinski, J. Golimowski, E. Bulska, B. Krasnodebska-Ostrega, R. Marassi, S. Zamponi, J. Electroanal. Chem. 460 (1999) 30.
[44] M. Grden, A. Piascik, Z. Koczorowski, A. Czerwinski, J. Electroanal. Chem. 532 (2002) 35.
[45] R. Hoyer, L.A. Kibler, D.M. Kolb, Electrochim. Acta 49 (2003) 63.
[46] H.F. Waibel, M. Kleinert, L.A. Kibler, D.M. Kolb, Electrochim. Acta 47 (2002) 1461.
[47] F.C. Nart, W. Vielstich, in: W. Vielstich, H.A. Gasteiger, A. Lamm (Eds.), Handbook of Fuel Cells—Fundamentals, Technology and Applications, vol. 2, John Wiley & Sons, 2003 (Chapter 21).
[48] V. Stamenkovic, T.J. Schmidt, P.N. Ross, N.M. Markovic, J. Electroanal. Chem. 554 (2003) 191.
[49] V. Stamenkovic, T.J. Schmidt, P.N. Ross, N.M. Markovic, J. Phys. Chem. B 106 (2002) 11970.
[50] M.Y. Rusanova, P. Polaskova, M. Muzikar, W.R. Fawcett, Electrochim. Acta 51 (2006) 3097.
[51] D.M. Artymowicz, J. Erlebacher, R.C. Newman, Philos. Mag. 89 (2009) 1663.
[52] J. Snyder, J. Erlebacher, J. Electrochem. Soc. 157 (2010) C125.